JOURNAL OF GEOPHYSICAL RESEARCH, VOL. 101, NO. C11, PAGES 25,813–25,832, NOVEMBER 15, 1996

Ocean surface features and currents measured with synthetic aperture radar interferometry and HF radar

Hans C. Graber

Rosenstiel School of Marine and Atmospheric Science, University of Miami, Miami, Florida

Donald R. Thompson

Applied Physics Laboratory, Johns Hopkins University, Laurel, Maryland

Richard E. Carande[1]

Jet Propulsion Laboratory, California Institute of Technology, Pasadena

Abstract. This paper describes the results of the first quantitative comparison between high-resolution ocean surface current fields extracted from interferometric synthetic aperture radar (INSAR) measurements and those from an high-frequency (HF) ocean surface current radar (OSCR) system. Data from each of these radar systems along with supporting measurements from shipboard and buoy-mounted sensors were collected during the High-Resolution Remote Sensing Experiment (High-Res) on June 20, 1993, on the continental shelf off the coast of Cape Hatteras, North Carolina. Both components of the surface current were obtained from the INSAR system at roughly 10-m resolution from two orthogonal flight legs over the region separated in time by about 30 min. The OSCR system measured two-dimensional surface current vectors at about 1-km resolution over this same region, while the USNS *Bartlett* was collecting hydrographic samples and near-surface current measurements. Two-dimensional wave spectra as well as meteorological and additional current measurements were collected at two buoys within the experimental area. We discuss in the paper two techniques for eliminating the effect of surface wave motion on the INSAR current estimates. One method relies on some knowledge of the local wind and wave field and the use of a microwave scattering model. The other method makes use of a few in situ current measurements spaced at different range locations across the INSAR image. Using either of these techniques, we find that the agreement between the INSAR and OSCR current estimates is generally very good. Furthermore, the INSAR current and magnitude imagery show the presence of undulating surface features where abrupt changes in the current speed and direction occurred. The ship surveys indicate that these features were caused by the collision of water masses of different density. We show for the first time in this paper a high-resolution, area-extensive vector surface current map derived from the INSAR of the two-dimensional flow in the vicinity of these features. Our results demonstrate convincingly that high-resolution oceanic surface current vectors can be derived from INSAR current measurements and that these measurements may be very beneficial for detailed studies of the dynamics of small-scale surface features in regions of strong current divergences or shears.

1. Introduction

Observations of mesoscale features by synthetic aperture radar (SAR) are plentiful in the literature. In particular, SEASAT SAR images and more recently ERS 1 SAR images of the ocean have provided ample evidence of such features as internal waves, current boundaries and shears, current and temperature fronts, eddies, and tidal flow over varying bathymetry [e.g., *Beal et al.*, 1981; *Fu and Holt*, 1982; *Beal et al.*, 1996]. Further support for detecting mesoscale features can be found not only in images from the shuttle missions SIR A [*Cimino and Elachi*, 1982; *Ford et al.*, 1983] and SIR B [*Ford et al.*, 1986; *Gasparovic et al.*, 1986; *Cimino et al.*, 1988] but also from shuttle Sun-glitter photography, for example, by *Scully-Power* [1986] and *La Violette et al.* [1990]. Unfortunately, concurrent ground-truth measurements of relevant air-sea interaction and oceanic parameters were rarely or never available for understanding quantitatively the responsible processes validating models of the image mechanisms. Several experiments have been carried out to study, for example, the influence of internal waves on the SAR imaging mechanism where in situ sea truth was coincident with airborne SAR overflights. (See, for example, Georgia Strait and SAR Internal Wave Signature Experiments special section, *Journal of Geophysical Research*, *93*(C10), 12,217–12,380, 1988.) It was found in these studies that models using relevant ground truth as input could explain quantitatively the main features found in the radar images. An accurate spatial representation of the ocean surface current

[1]Now at Vexcel Corporation, Boulder, Colorado.

Paper number 96JC02241.
0148-0227/96/96JC-02241$09.00

induced by the internal wave field was found to be one of the more important quantities required for the initialization of these imaging models.

Recently, numerous small-scale eddies were observed with a shore-based high-frequency (HF) Doppler radar in an experiment off the South Florida Keys [*Graber et al.*, 1995]. These eddies traversed the illuminated field of view of the radar on a timescale of approximately one every 3 to 5 days. These surface features were easily detected in the radar vector current maps and provided the first synoptic observations of vortex-like circulation features with a small diameter of about 10–30 km and swirl speeds of 0.1–0.5 m s^{-1}. *Lee* [1975] first observed these disturbances when strong cyclonic reversals appeared in current meter records, and he described these features as cyclonic edge eddies or spin-off eddies which form along the inshore edge of the Florida Current. The data suggest that the evolution of these spin-off eddies is caused by dynamical instabilities of the Florida Current which may be originally wind induced [*Lee and Mayer*, 1977]. The path of these spin-off eddies was generally along the 150-m isobath, and their propagation speed was about 1 km h^{-1} or ~0.25 m s^{-1}. Observations of the space-time evolution of mesoscale and submesoscale features such as these eddies are only possible with high-resolution measurements provided by radars. For example, knowledge of the spatial and temporal variations of the two-dimensional current field has proved to be crucial for interpreting the recruitment and dispersal mechanisms of tropical reef fish larvae (H. C. Graber et al., Spin-off eddies: The rapid transportation system of tropical reef fish larvae, submitted to *Journal of Marine Research*, 1996).

Marmorino et al. [1994] discussed a surface convergence feature imaged with an airborne SAR and sampled by shipboard sensors. The shipboard hydrographic measurements indicated a distinct boundary between a filament of cool, fresh water and warm, salty Gulf Stream water. The frontal feature appeared in the SAR image as a narrow line with backscatter strength 1–2 dB higher than the surrounding area. Model calculations based on composite radar backscattering with inclusion of observed wave breaking distributions were in good agreement with the SAR observations. Again, in this example it was found that higher-resolution measurements of the strain rate and shear associated with the feature are necessary to improve estimates of surface roughening by wave-current interaction effects.

In each of the examples discussed above, ocean surface currents are an important process in modifying the short gravity waves that are primarily responsible for the backscattering of microwave radiation and hence the intensity modulations observed in the imagery. Bright features are often observed in airborne and spaceborne radar imagery in regions where variable currents lead to focusing and steepening of the local shortwave field. Because of their complicated two-dimensional structure and the fact that they are usually not fixed in space, it is very difficult to characterize these current fields using measurements from point sensors. Traditional in situ surface current measurement techniques are subject to errors associated with the invasive nature of the sensor systems. Current records from surface drifters and measurements from taut moorings can be biased by wind and wave action as well as flow distortion due to the presence of the instruments in the current field. Drifters can vary in shape and size and thus respond differently to flow variations with depth. Furthermore, maintaining current meters near the water surface is difficult, especially in highly sheared flow and large fluctuating velocities. Noninvasive remote-sensing techniques using radar systems can overcome many of these difficulties. Numerous experiments have been carried out with HF radar systems as an alternative approach for surface current measurements, especially in regions of high-velocity shear, for example near the Gulf Stream or regions of large tidal ranges [e.g., *Shay et al.*, 1993; *Graber et al.*, 1995]. These systems can provide accurate maps of surface current fields at a resolution of the order of 1 km as a function of time. Such a time series is very useful for locating ocean features and for measuring and quantifying the associated space-time variability of the surface current field. It is possible that interferometric SAR (INSAR) [*Goldstein and Zebker*, 1987] can complement the HF measurements through the measurement of area-extensive surface current imagery at very high spatial resolution. INSAR current measurement is a relatively new technique, and the few previous attempts to quantitatively validate its use have suffered from the lack of ground truth data [*Ainsworth et al.*, 1995; *Shemer et al.*, 1993]. We believe that the results to be presented in this paper will go a long way toward remedying this situation. With convincing validation of INSAR measurements, their use in conjunction with HF systems in the coastal and inner shelf regions offers a unique method to observe in real time the spatial and temporal variation of surface flow patterns.

As part of the High-Resolution Remote Sensing Experiment (High-Res) research program [*Herr et al.*, 1991], a field experiment was conducted in June 1993 off the outer banks of North Carolina. The general objective of the High-Res program was to understand the physics responsible for the appearance of mesoscale and submesoscale oceanographic features in microwave images of the coastal ocean. The focus of the program's experimental effort was on the inshore edge of the North Wall of the Gulf Stream (see the map in Figure 1). This location provides a regime rich in mesoscale oceanic variability where the effects of current shear and vorticity, thermal jumps, and surface roughness can be examined and the generation mechanisms of submesoscale oceanic features explored. The possibility of obtaining extensive ground-truth data during High-Res provided a unique opportunity to validate not only INSAR current measurements but measurements from the HF system as well. In this paper we concentrate mainly on the INSAR validation, while comparisons of the HF-derived currents with in situ measurements have been reported in recent papers by R. D. Chapman et al. (The accuracy of HF radar current measurements, submitted to *Journal of Geophysical Research*, 1996) (hereinafter referred to as Chapman et al., submitted manuscript, 1996) and H. C. Graber et al. (HF radar comparisons with moored estimates of current speed and direction: Expected differences and implications, submitted to *Journal of Geophysical Research*, 1996; hereinafter referred to as Graber et al., submitted manuscript, 1996). These latter papers have shown that the HF currents agree quite well with shipboard acoustic Doppler current profiler (ADCP) and buoy-mounted current measurements, respectively. Thus in the present paper we will treat the HF measurements as ground truth for the validation of the INSAR-derived currents.

In section 2 we describe the experimental setup and sensors used during the High-Res field program. A discussion is given in section 3 of how surface currents are extracted from the HF and INSAR radar systems. Here particular attention will be paid to the removal of biases from the INSAR system due to navigation uncertainties and wave and wind effects. A compar-

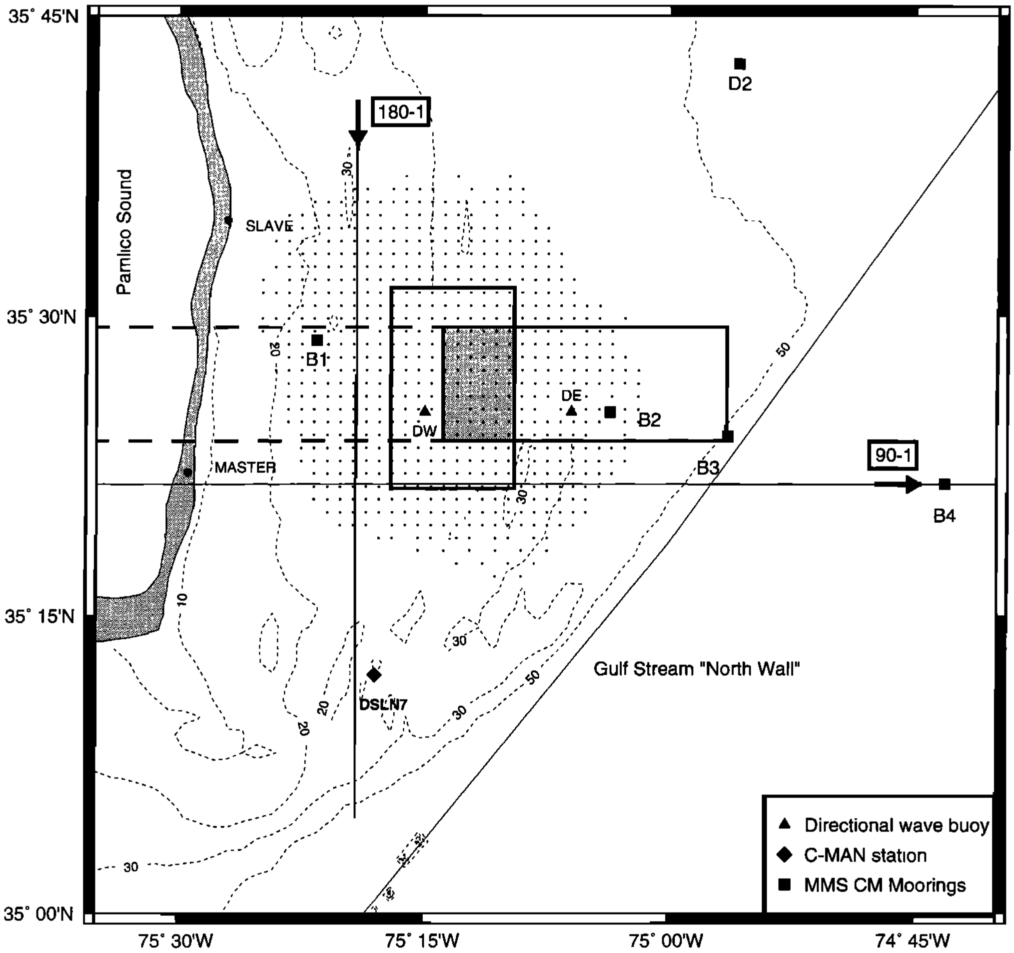

Figure 1. Map of the High-Res experimental area. The arrows indicate flight lines of the NASA DC 8, and the rectangles show part of the area imaged on the 90-1 and 180-1 flight legs. The small solid dots indicate the coverage area of the OSCR HF radar system. The shaded rectangle shows the area common to both flight legs. Bottom topography contours (meters) are displayed by dashed lines, and the climatological mean position of the Gulf Stream North Wall is also shown.

ison of the remotely sensed surface current fields from the HF radar and INSAR system is presented in section 4 along with a brief discussion of a high-resolution map obtained from the INSAR of the flow field in the region of a mesoscale surface feature sampled during High-Res. The results of our investigation are summarized in section 5, and concluding remarks are given in section 6.

2. Experimental Setting and Sensors During High-Res

A special data set was collected on June 20, 1993, over the continental shelf region off the coast of Cape Hatteras, North Carolina, during the High-Res experiment sponsored by the Office of Naval Research (ONR) and the Naval Research Laboratory (NRL). Phase maps were generated over this region by the L band INSAR flown on board the NASA DC 8. These phase maps may, under the proper conditions, be converted to estimates of the surface current component in the INSAR look range direction. Roughly 1 hour later, the same area was imaged in the standard strip-map mode by the trifrequency (P, L, and C band) SAR mounted on the same platform. Concurrent with the DC 8 data collection, a shore-based HF ocean surface current radar (OSCR) operated by the University of Miami [*Shay et al.*, 1995] also measured two-dimensional surface current vectors at approximately 1-km resolution out to roughly 45 km offshore. Two wave buoys moored in the area provided wind and wind stress, directional wave spectra, and near-surface currents at about 10-m depth. Finally, the research vessels USNS *Bartlett* and R/V *Columbus Iselin* collected a wide variety of concurrent in situ measurements including along-track currents and density profiles. A major research goal of this investigation is to validate the INSAR and HF radar current measurements with those from the more conventional (but less area extensive) instruments and utilize these remote sensing techniques to study radar modulations in the presence of mesoscale surface features.

Figure 1 shows a map of the High-Res experiment area off Cape Hatteras. The OSCR "master" and "slave" stations were located at Avon and Waves, North Carolina, respectively [*Shay et al.*, 1995]. The OSCR coverage and cell locations are shown by the circular dots centered between these stations. The arrows seen in Figure 1 delineate the flight directions of two of the four passes of the DC 8 on June 20. Both INSAR and strip-map SAR data were collected along each leg of the two tracks within an interval of about 1 hour. The rectangles in the

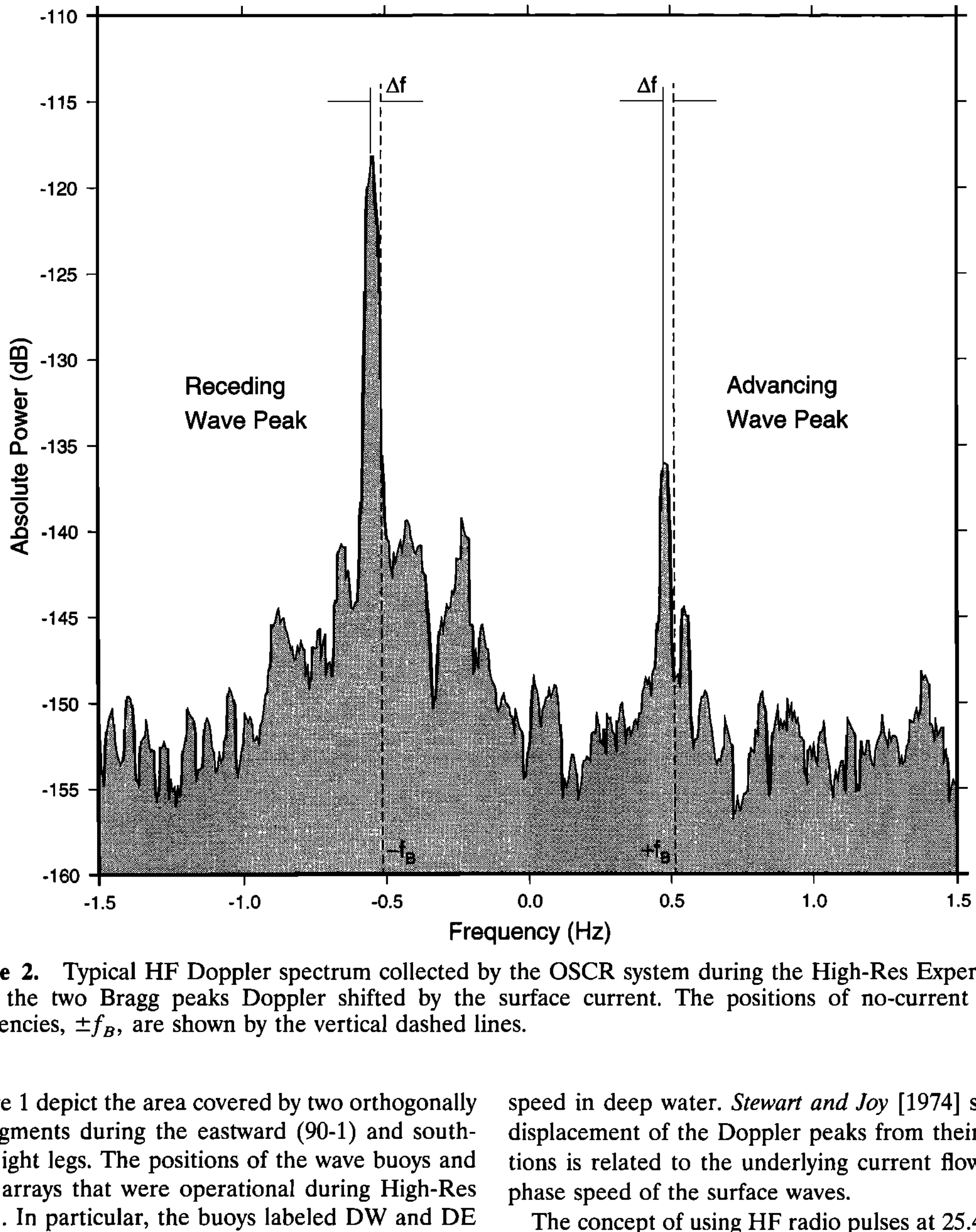

Figure 2. Typical HF Doppler spectrum collected by the OSCR system during the High-Res Experiment. Note the two Bragg peaks Doppler shifted by the surface current. The positions of no-current Bragg frequencies, $\pm f_B$, are shown by the vertical dashed lines.

center of Figure 1 depict the area covered by two orthogonally overlapping segments during the eastward (90-1) and southward (180-1) flight legs. The positions of the wave buoys and current meter arrays that were operational during High-Res are also shown. In particular, the buoys labeled DW and DE near the lower edge of the SAR area were capable of measuring the directional energy spectrum of the long surface waves as well as standard meteorological measurements. These two buoys were also equipped with vector current meters moored about 10 m below the surface.

2.1. Ocean Surface Current Radar

A promising method for measuring vector surface currents that has evolved over the past 4 decades is the Doppler radar technique originally described by *Crombie* [1955], who observed that the echo Doppler spectrum from an HF radar system consists of two distinct, narrow peaks positioned nearly symmetrically about zero frequency (Figure 2). The concept is based on the premise that radar pulses are backscattered from the moving ocean surface by resonant surface waves ("Bragg waves") whose wavelength is one half of the radar wavelength. The two spikes resulting from Bragg resonant scattering originate from two targets moving at constant velocity on the ocean surface, one toward and the other away from the radar. Ocean surface gravity waves of given wavelength travel at a constant speed in deep water. *Stewart and Joy* [1974] showed that the displacement of the Doppler peaks from their expected positions is related to the underlying current flow modifying the phase speed of the surface waves.

The concept of using HF radio pulses at 25.4 MHz to probe the ocean surface to deduce near-surface currents has received considerable attention in coastal oceanographic experiments. The shore-based radar system consists of two units (master and slave) which are deployed at tens of kilometers apart. Each unit makes independent measurements of current speed along radial beams emanating from its phased-array antennae system. The data are then combined via UHF or telephone communication to produce vector currents (speed and direction), stored on disk, and displayed in near real time. The measurements can be made simultaneously at up to 700 grid points at 1-km resolution. The measurement cycle for each vector current map is repeated every 20 min. The main specifications and capabilities of the OSCR system are listed in Table 1.

The Rosenstiel School of Marine and Atmospheric Science OSCR radar system (developed by MAREX Technology, Ltd.) was deployed for a jointly sponsored ONR/Minerals Management Service (MMS) study along Cape Hatteras from June 11 to July 8, 1993. The system consisted of two HF radar transmit/receive stations operating at 25.4 MHz, thereby providing information on scattering mechanisms at gravity wavelengths of about 6 m (Table 1). The HF radar system mapped the coastal ocean currents over a 30 × 45 km domain at 20-min intervals with a horizontal resolution of about 1.2 km. The individual radars were located at two ocean front sites in Avon and Waves, North Carolina. The baseline separation between these two sites amount to 24 km. Each site consisted of a four-element transmit and 16-element receiving array oriented at an angle of about 30° to the beach front (SE-NW at Avon and NE-SW at Waves) over a distance of 85 m. Communications between the two stations were facilitated by a UHF radio link.

2.2. Interferometric Synthetic Aperture Radar

On June 20, 1993, the NASA DC 8-72 airborne laboratory flew a dedicated mission over the shelf waters off Cape Hatteras. On board the aircraft were Jet Propulsion Laboratory's SAR sensors operating at P, L, and C band frequencies and the L band interferometric SAR (INSAR). The flight mission began near Duck, North Carolina, and followed the coastline to the High-Res experimental area. The flight pattern consisted of four legs oriented toward east, west, south, and north. This flight pattern was first flown in the INSAR mode and then repeated about 1 hour later in the trifrequency SAR mode. The experimental objective of this flight was to obtain simultaneous measurements of polarmetric and interferometric backscatter within the domain covered by the HF Doppler radar and near the directional wave buoys. Relevant system and flight parameters are presented in Table 1.

On flight leg 180-1 (aircraft heading 180°) the SAR imaged a distinct surface feature located east of buoy DW. About 30 min later, the eastbound flight leg 90-1, originating over Pamlico Sound (compare Figure 1), revealed that this undulating surface feature also extended in an east-west direction and separated two flow regimes which converged along its irregular boundary. Note that this flight segment, 90-1, also included a section of flat terrain of the Outer Banks. As will be discussed in the next section, the imaging of land was important for removing the navigational bias in the INSAR phase image.

2.3. Buoy and Ship Instrumentation

During the High-Res experiment, several additional research platforms acquired measurements in the OSCR domain. These platforms included the research vessels R/V *Columbus Iselin* and USNS *Bartlett*, moored buoys, and aircraft from the NRL, the Naval Air Development Center, as well as a spotter plane. Of particular relevance were the upper ocean current profiles measured by the 300- and 1200-KHz ADCPs from the *Bartlett* and *Columbus Iselin* and the moored current meters at the two discus buoys, labeled DE and DW in Figure 1. The two modified 3-m discus buoys measured both atmospheric and oceanic variables as well as the directional energy spectrum of surface gravity waves [*Anctil et al.*, 1993].

The ships made periodic transects through the OSCR illuminated field of view not only facilitating direct comparison of the ADCP data with the surface current vectors at several locations (*Chapman et al.*, submitted manuscript, 1996), but also detecting and sampling frontal features. A 1200-KHz ADCP provided high vertical resolution current profiles in the upper 2–5 m of the water column. A single current meter about 10 m below the surface provided time series observations of three-dimensional currents, water temperature, density, and conductivity at the two discus buoys.

Table 1. Specification of OSCR (HF) and INSAR (L Band) Radar System Parameters During High-Res on June 20, 1993

Parameter	OSCR	INSAR
Frequency	25.4 MHz	1.25 GHz
Ground resolution	1 km	10 m
Range or swath width*	45 km	8.2 km
Altitude	0 (land)	8.5 km
Flight speed	NA	~200 m s^{-1}
Incidence angle	90°	25°–55°
Bragg wavelength	6 m	24 cm
Antenna separation	16 × 6 m	20 m
Measurement cycle	20 min	NA
Measurement depth	~40 cm	~1 cm
Accuracy radial current	~2 cm s^{-1}	~1 cm s^{-1}

*Value depends on setup geometry or flight altitude.

3. Remotely Sensed Surface Currents

3.1 HF Radar Measurements

The measurement of ocean surface currents by HF Doppler radar techniques is based on the fact that for HF radar frequencies (10- to 100-MHz range), the rms height of the ocean surface is much less than the wavelength of the impinging radiation. When this condition is satisfied (the so-called Bragg condition), the scattering physics is determined (for backscatter geometry) by the spectral components or "Bragg waves" of the wave-height spectral density, $\Psi(\mathbf{k})$, whose wavenumber k_B (the Bragg wavenumber) is given by

$$k_B = 2k_r \sin \theta_i, \tag{1}$$

where $k_r(=(2\pi/\lambda r))$ is the radar wavenumber and θ_i is the radar incidence angle. For the OSCR system employed in this study, $\lambda_r = 11.8$ m corresponding to a frequency of 25.4 MHz, and θ_i is 90°, so k_B for this case is equal to twice the radar wavenumber or to one half the radar wavelength (i.e., 5.9 m). Thus the scattering will satisfy the Bragg condition for all but the highest sea states. When the Bragg condition is satisfied, the autocovariance of the backscatter power, $R_B(t)$, may be written as

$$R_B(t) = 8\pi k_r^4 g_p(\theta_i)\{\Psi(\mathbf{k}_B) \exp[-i(\omega_B + \mathbf{k}_B \cdot \mathbf{V})t] + \Psi(-\mathbf{k}_B) \exp[i(\omega_B - \mathbf{k}_B \cdot \mathbf{V})t]\}. \tag{2}$$

where the function $g_p(\theta_i)$ depends on the incidence angle and the polarization p of the radiation [*Plant*, 1990]. The quantity, ω_B, appearing in (2) is the radian frequency of a surface wave whose wavenumber is k_B. For linear waves, ω_B is given by

$$\omega_B = 2\pi f_B = \sqrt{g k_B[1 + (k_B/k_s)^2] \tanh(k_B h)}, \tag{3}$$

and the corresponding Bragg phase speed is

$$C_B = \omega_B/k_B. \tag{4}$$

In (3), g is the gravitational acceleration, h is the water depth, and k_s equals $\sqrt{\tau_s/\rho g}$ with τ_s being the surface tension and ρ the fluid density. For seawater, $k_s \simeq 363$ rad m^{-1}. Included in the expression for the Bragg autocovariance function in (2) is the effect of a local background surface current, $\mathbf{V}$, that can Doppler shift the frequency of the Bragg waves by an amount $\mathbf{k}_B \cdot \mathbf{V}$. We will see below how the frequency shift in HF Doppler spectra can be used to measure $\mathbf{V}$. Finally, one should note that $R_B(0)$ in (2) gives the backscattered power in the Bragg limit and that $R_B(t)$ depends on the spectral density of Bragg spectral components propagating both toward and away from the radar.

The autocovariance of the backscattered field is related to the Doppler spectrum, $S(\omega)$, through the Fourier transform in the usual way by

$$R(t) = \frac{1}{\sqrt{2\pi}} \int_{-\infty}^{\infty} e^{i\omega t} S(\omega)\, d\omega. \tag{5}$$

where $S(\omega)$ is a real band-limited function since $R(t)$ is Hermitian and, in general, is not symmetric about $\omega = 0$. A typical Doppler spectrum from the OSCR system deployed in High-Res is shown in Figure 2. As mentioned in the previous section, HF Doppler spectra generally exhibit two sharp discrete spectral peaks at positive and negative frequencies such as those seen in Figure 2. It can be seen from (2) that in the absence of a surface current, **V**, the Doppler spectrum will be symmetric about zero with the spectral peaks located at the frequencies, $\pm f_B$. These frequencies are shown by the dashed vertical lines in Figure 2. If there is an underlying surface current with component V_r along the look direction of the radar, the Bragg peaks in the Doppler spectrum will still be separated by a frequency difference of $2f_B$ as in the no-current case, but as shown in Figure 2, both peaks will be shifted by the amount

$$\Delta f = \frac{\mathbf{k}_B \cdot \mathbf{V}}{2\pi} = \frac{2V_r}{\lambda_r} \tag{6}$$

for $\theta_i = 90°$. Using equation (6), one can now compute V_r from measurements of Δf.

To determine both components of two-dimensional surface current fields (magnitude and direction), two radar HF stations are required, and their baseline separation determines the domain of the mapped region. The radial velocity along the look direction from each station is measured, and the two values are then projected onto a convenient orthogonal coordinate system. It is clear that the intrinsic error in this procedure depends on the angle between the respective look directions. In particular, if this angle is small, then error in the derived surface current component that is nearly orthogonal to the radial components from both stations can be significant. For more details of this procedure, see, for example, *Graber et al.* (submitted manuscript, 1996). It should be mentioned that although HF radar systems have been operational for many years [*Barrick et al.*, 1983] and the operating principle appears to be straightforward, there are, in fact, many subtleties involved in their operation. It is intended that the comparison between OSCR and INSAR surface currents presented in this study and comparisons with other measurements [*Shay et al.*, 1995; Graber et al., submitted manuscript, 1996; Chapman et al., submitted manuscript, 1996] will help to better understand some of these subtleties.

3.2. Interferometric SAR Measurements

The NASA Jet Propulsion Laboratory (JPL) DC 8 aircraft includes two fuselage-mounted L band antennae separated by a distance D of 20 m. When operating in the interferometer mode, a pulse is transmitted from the aft antenna and received on both the forward and aft antennae. Individual complex SAR images are formed using both antennae. When the aircraft is flying at the nominal speed, V = 200 m s^{-1}, the lag time τ between the forward and the aft antenna images is given by

$$\tau = \frac{D}{2V} \approx 0.05 \text{ s}. \tag{7}$$

The divisor of 2 is a result of the fact that transmission occurs only at the aft antenna. During High-Res it was possible to transmit only from the aft antenna. (Recently, the INSAR system has been modified to allow transmission from both the fore and aft antennas. For this latter configuration the factor of 2 no longer appears in the denominator of (7) [*Carande*, 1993]. Thus with the appropriate processing, two lag times of approximately 0.05 s and 0.10 s are available with this new configuration.) The lag time must be smaller than the decorrelation time of the L band backscattered field ($\approx$0.3–0.4 s for light to moderate winds [*Plant*, 1990]). If τ is larger than the decorrelation time, no phase information can be obtained from the interferometric measurements.

When τ is small enough, one can measure the pixel-by-pixel phase difference, ϕ, between the two (complex) SAR images from the forward and aft antennas. This quantity is equal to the phase of the autocovariance function, $R(\tau)$, of the field backscattered from each pixel at lag time τ; that is,

$$\phi = \arg\{R(\tau)\}. \tag{8}$$

where $R(\tau)$ is given by

$$R(\tau) = E\{B(t)B^*(t-\tau)\}, \tag{9}$$

and $E\{\ \}$ denotes ensemble average and $B(t)$ is the backscattered field from a particular pixel at time t. The autocovariance function in (9) is the same quantity discussed in section 3.1 in connection with the OSCR system. As we will see below, however, $R(\tau)$ for the INSAR system in general cannot be written in the form given by (2) since L band backscatter from the ocean surface usually does not satisfy the Bragg condition [*Thompson*, 1989]. The autocovariance function measured from the INSAR is nevertheless still related to the Doppler spectrum, $S(\omega)$, through (5). Furthermore, if $\omega\tau \ll 1$ over the frequency band of $S(\omega)$, then we may approximate (5) by

$$R(\tau) \approx \frac{1}{\sqrt{2\pi}} \int_{-\infty}^{\infty} (1 + i\omega\tau) S(\omega)\, d\omega. \tag{10}$$

In this approximation, the phase of $R(\tau)$ $(=\phi)$ is given by

$$\phi = \tau \frac{\int_{-\infty}^{\infty} \omega S(\omega)\, d\omega}{\int_{-\infty}^{\infty} S(\omega)\, d\omega} = \bar{\omega}\tau, \tag{11}$$

where $\bar{\omega}$ is the mean Doppler frequency. Equation (11) states that the pixel-by-pixel phase difference measured by the INSAR (which is equal to the phase of $R(\tau)$ at lag time τ) is proportional to the mean Doppler frequency $\bar{\omega}$.

If the phase of $R(\tau)$ is due to simple horizontal advection of the scatterers, as argued by *Goldstein and Zebker* [1987] and *Goldstein et al.* [1989], then ϕ, measured by the INSAR, can be used to infer the variation of the horizontal surface velocity field, V_{in}, in the radar look direction on a pixel-by-pixel basis across the INSAR image using the relation

$$V_{in} = \frac{\phi}{\tau k_B}, \tag{12}$$

where k_B is given by (1) with the appropriate L band parameters. The quantity V_{in} defined here is, in principle, the same as the surface velocity field, V, discussed in section 3.1. We have chosen to distinguish explicitly the OSCR and INSAR measurement techniques by using the subscript "*in*" for the INSAR-measured surface current field. Although it was shown in a previous study [*Thompson and Jensen*, 1993] that special cases do exist where (12) is not valid, we nevertheless believe that with the proper precautions, this equation can provide reliable estimates of the surface current field. It is one of the primary goals of this study to verify (12) using comparisons between OSCR and INSAR currents measured during High-Res.

3.2.1. Platform navigation effects. In deriving (7), it is implicitly assumed that the INSAR platform is flying at a constant velocity and that its velocity vector is oriented in exactly the same direction as the heading vector (i.e., the vector directed along the fuselage of the aircraft). This assumption is almost never exactly valid under actual flight conditions, and failure to properly account for this "nonalignment" can cause a significant bias in the INSAR phase as a function of range across the image. A further range-dependent bias results when the platform altitude is not accurately known. These navigation and attitude effects can, in principle, be accounted for by the Global Positioning System (GPS) system on board the airborne SAR (AIRSAR) platform. During the High-Res experiment, however, this system was not yet completely functional, and so the nonalignment and altitude biases had to be accounted for by other means.

For the eastbound 90-1 pass discussed in section 2 the flight track was perpendicular to a section of the Outer Banks that is oriented along a nearly north/south direction (see the map in Figure 1). Since we know that there are no significant elevation changes over this region and that there is also no horizontal velocity, we can effectively determine the range dependence of the navigational bias as the equivalent range-dependent phase trend that forces the measured phase difference to be zero at each range (latitude) location along the section of the Outer Banks. As seen in Figure 1, this section of the Outer Banks extends over only a few kilometers (0.02° or so) in longitude. The navigation correction is then simply the phase trend in latitude (smoothed over about 100 m in the latitude direction and averaged in longitude across the narrow strip of land). When this trend is subtracted from the measured values in the 90-1 phase image, the phase along the Outer Banks is zero by construction.

3.2.2. Wave-motion and wind-drift effects. Besides the phase trend due to platform navigation effects discussed in the previous section, there are also phase trends due to the fact that the ocean surface is moving. This surface motion is due to the shear layer at the air-sea interface, the so-called wind-drift layer, and to the motion of the surface waves themselves. Just as in the case of the OSCR system, the INSAR will respond to these wave- and wind-induced surface motions even when no ambient current field is present. Thus phase differences associated with such motions must be properly accounted for in order to measure the absolute magnitude of mesoscale and submesoscale surface currents with interferometric SAR systems.

Unlike the OSCR system discussed in section 3.1 which directly measures the peak frequency of both the advancing and receding Bragg waves in the Doppler spectrum (compare Figure 2), the INSAR system measures a phase difference that is related by (11) to the mean Doppler frequency weighted over the entire extent (positive and negative frequencies) of the Doppler spectrum. Also, since the microwave INSAR system operates at a wavelength of 24 cm, the total rms surface height will be significantly greater than the radar wavelength except for very low wind conditions. Hence the simple Bragg scattering physics discussed in section 3.1 in connection with the OSCR system will usually not be applicable. This means that the dynamics of the longer (and higher) surface waves will influence the Doppler spectrum and in particular that the mean Doppler frequency will in general not equal the Bragg frequency as in the case of the OSCR. Examples of how the orbital velocity of the long surface waves can affect the mean Doppler frequency are discussed by *Thompson* [1989] and also by *Thompson et al.* [1991], where comparisons are made between measurements and a time-dependent radar scattering model.

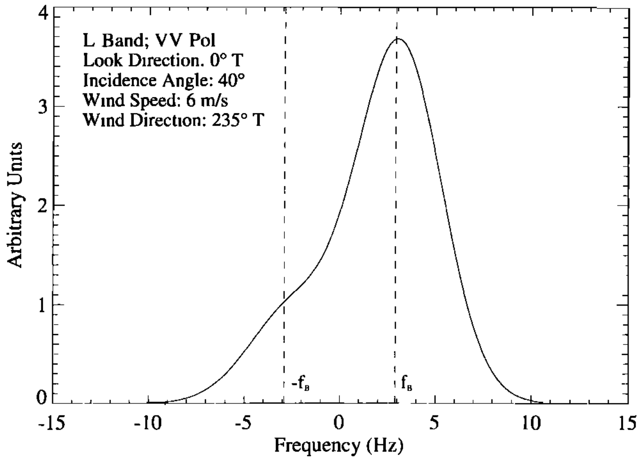

Figure 3. Computed L band Doppler spectrum for VV polarization, 40° incidence, 0° radar look direction, a wind speed of 6 m s^{-1}, and the wind direction from 235°. The dashed lines indicate the position of the positive and negative Bragg frequencies, $\pm f_B$.

Using this scattering model, we have computed mean Doppler spectra for an L band radar looking toward 0°T operating at vertical polarization over a range of incidence angles from 20° to 60° that corresponds approximately to the latitude extent of the INSAR swath shown in Figure 1. As an example we show the computed Doppler spectrum for 40° incidence in Figure 3. The dashed lines in this plot indicate the position of the positive and negative Bragg frequencies, $\pm f_B$, for the L band INSAR system. Comparing Figure 3 with the OSCR Doppler spectrum shown in Figure 2, we see that the L band spectrum is significantly broader and the two peaks corresponding to the advancing and receding Bragg waves are not nearly so distinct. The positive frequency peak is larger since for the chosen wind direction, there is more energy in the waves propagating away from the radar than toward it. (Note that we have chosen the phase convention that positive Doppler shifts indicate velocities directed away from the radar.) Only a small shoulder in the L band spectrum in Figure 3 indicates the position of the negative-frequency peak. Because of the broadness of the L-band Doppler spectra, the current measurement technique

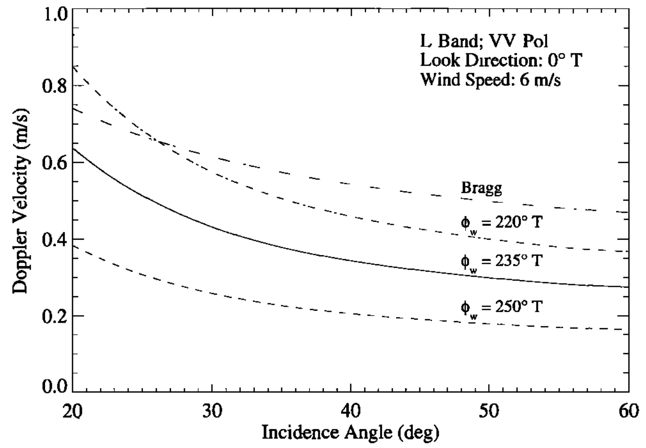

Figure 4. Computed L band Doppler velocities as a function of incidence angle for VV polarization and a radar look direction of 0°T. All computations are for 6 m s^{-1} winds. The curves labeled by ϕ_w show the computed results for the winds from the indicated direction. The curve labeled "Bragg" shows the dependence of the Bragg phase speed as a function of incidence angle.

used in the OSCR system based on the position of the spectral peak is not applicable.

The mean Doppler frequencies extracted from the computed spectra have been converted to apparent mean velocities using (11)–(12) and plotted as a function of incidence angle in Figure 4. For these computations we have used the wave spectral data and wind vector collected from a directional wave buoy in the experimental area at the INSAR overpass time. The structure of the shortwave field required by the model is derived from a wind-dependent model spectrum used in previous studies [*Thompson et al.*, 1991]. At the overpass time the measured wind speeds were about 5–6 m s^{-1} from 235°T at both the DE and DW wave buoys (compare Figure 1), which indicates that the meteorological conditions were fairly uniform. The solid curve in Figure 4 shows the mean Doppler velocity as a function of incidence angle computed using the observed wind data. The dashed and dot-dashed curves in Figure 4 show the corresponding mean Doppler velocities when the wind direction, ϕ_w deviates by $\pm 15°$ from the mean direction. One can see from these curves that the mean Doppler velocity decreases as the angle between the wind direction and the radar look direction (toward 0°T) increases. This is expected since the relative contributions to the velocity of the advancing and receding waves along the radar look direction become more nearly equal as this angle increases. When the wind and radar are perpendicular, the mean Doppler velocity will be essentially zero. The curve labeled "Bragg" in Figure 4 shows the phase velocity of an L band Bragg wave (propagating away from the radar). Notice that the Bragg phase velocity curve decreases more slowly with incidence angle (especially in the smaller incidence-angle regime) than do the computed mean Doppler velocities. This slower decrease is due primarily to the effect of surface waves longer than the Bragg waves and to the two-dimensional character of the surface wave spectrum. Also, it is interesting to note that the three mean Doppler velocity curves (labeled by ϕ_w values in Figure 4) have nearly the same shape over the entire incidence angle range and are thus roughly equivalent to within a scaling constant. This rough equivalence will be useful later on in our discussion of absolute calibration of the INSAR system.

It should be mentioned here that the Doppler velocity curves shown in Figure 4 were computed using (12) with the phase, ϕ, computed using the approximate expression (11) for the mean Doppler frequency, $\bar{\omega}$. We have checked the validity of this approximation by comparing the phase values from (12) with the phase of $R(\tau)$ (for $\tau = 0.05$ s) taken directly from our scattering model. These two values were found to agree to within about 10%. More important is the fact that incidence-angle dependence of the Doppler velocities computed using the "exact" phases is virtually the same as those computed with the approximate expression of (12). Given this equivalence of the incidence-angle dependence and since, as we will discuss below, we cannot hope to calculate the absolute velocity correction better than about 10% without at least one additional independent velocity measurement, we feel that the approximate expression for the mean Doppler frequency given by (12) is sufficient for our investigation.

The differences in the computed mean velocities shown in Figure 4 are a reflection of the sensitivity of the computations not only to the actual wind direction but also to the form of the particular angular spreading function used in our model spectrum, which is assumed to be symmetric about the wind direction. For a given radar look direction with respect to the wind, a wave spectrum with a broad spreading function implies that the spectral components of waves propagating toward or away from the radar are more equal than for a narrow spreading function. Thus for a fixed look direction a broad spectrum will generally yield smaller mean Doppler velocities than will a narrower spectrum. Also, we should mention here that in our model calculations, the mean Doppler velocity is influenced most strongly by those spectral components whose wavelengths are shorter than 10 m. Unfortunately, these waves are shorter than the cutoff wavelength of the wave buoys.

The Doppler velocity curves shown in Figure 4 provide an estimate of the expected velocity trend in the INSAR image due to surface-wave motion effects. As mentioned earlier, there is also a so-called wind-drift velocity at the air-sea interface that must be included in the final INSAR calibration. This wind-drift velocity is usually estimated to be about 3% of the 10-m wind speed. For the conditions of the 90-1 INSAR pass of interest here (winds of $\approx$6 m s^{-1} from 235°T), the above estimate yields a wind-drift component along the INSAR look direction of about 0.1 m s^{-1}. This term will contribute an additional constant offset to the mean Doppler velocities shown in Figure 4.

3.2.3. Total cross-track velocity trend. We are now in a position to estimate the total cross-track velocity trend that must be removed from the INSAR phase image in order to obtain absolute velocity measurements. To accomplish this, we must combine the navigation trend that zeros the phase along the Outer Banks as discussed in subsection 3.2.1 with the mean Doppler velocity corrections computed from our model as discussed above in subsection 3.2.2 and remove this total velocity trend from the INSAR image. The basic steps in this procedure are outlined below.

The range-dependent navigational phase trend that forces the phase values to be zero along the Outer Banks has been converted to velocity using (12) and is shown as a function of latitude by the long-dashed curve labeled V_{nav} in Figure 5. The latitude range shown in Figure 5 corresponds roughly to incidence angles between 20° and 60° and encompasses the swath width of the INSAR system during the eastbound 90-1 pass. One can see that the navigational correction accounts for about 1 m s^{-1} variation in velocity over the entire swath width. Thus this correction is a very important part of the INSAR calibration. To complete the calibration procedure, the surface wave motion contribution, V_{ϕ_w}, must be subtracted from the navigational correction, V_{nav}. The results of this operation for the three wind-dependent mean Doppler velocities, computed as discussed above, are displayed in Figure 5. For comparison the curve resulting from the navigational correction minus only the Bragg velocity, $V_{\text{nav}} - C_B$, is also presented in Figure 5.

The wind-drift contribution, which as discussed above for the case of interest here, would subtract an additional constant velocity of about 0.1 m s^{-1} from each curve. This contribution is excluded in the curves shown in Figure 5 because the velocity spread due to uncertainties in the wind direction and/or the directional distribution of the shortwave spectrum is already more than this amount. It is, however, easy to see that this additional wind-drift correction would simply shift the curves down by 0.1 m s^{-1} (i.e., removing a positive wind-drift component).

In order to assess how well we have been able to calibrate the INSAR system, we will now show a comparison with OSCR-measured velocities. As will be discussed in more detail in the following section, we facilitate this comparison by smoothing the INSAR data to 1 × 1 km cells to match the OSCR system's intrinsically lower resolution. The symbols labeled "OSCR correction" in Figure 5 are the velocity values (no navigation or wave-motion corrections) that must be added to the "raw" (smoothed) INSAR velocity values to bring them into agreement with the corresponding OSCR components located at the westernmost longitude (−75.23°) and the latitude locations indicated in the figure. No averaging over longitude or formal minimization was performed in the determination of these values. We have simply chosen values that, when added to the raw INSAR velocities, bring them into general agreement with the corresponding OSCR values. We have chosen the OSCR measurement locations nearest to shore (westernmost longitude in the 90-1 image) to define the "OSCR correction" points since these OSCR measurements have a smaller error in the north velocity components than do points further to the east. The determination of these "OSCR correction" points defines another independent methodology for removing the range-dependent trends in the INSAR data. This methodology requires several independent velocity measurements spaced across the range extent of the INSAR image but eliminates the need for navigational and wind-dependent corrections.

It is quite encouraging that our "OSCR corrections" are bracketed by the $V_{\text{nav}} - V_{235}$ and $V_{\text{nav}} - V_{250}$ curves in Figure 5. Note also that the velocity trend defined by the "OSCR correction" exhibits nearly the same dependence with latitude as does the trend shown by the three wind-dependent curves. These latter curves were deduced using the methods described above which depend most strongly on the wind direction and angular spreading of the surface wave spectrum and are independent of any knowledge of the ambient surface-current field. Thus we have a self-consistency check for both the OSCR and the INSAR systems, and the close agreement of the velocity trends determined by these two techniques provides additional confidence in our understanding of the relevant physics. From Figure 5 we see that a Doppler velocity correction based on a computation for which $\phi_w \approx 242°$T

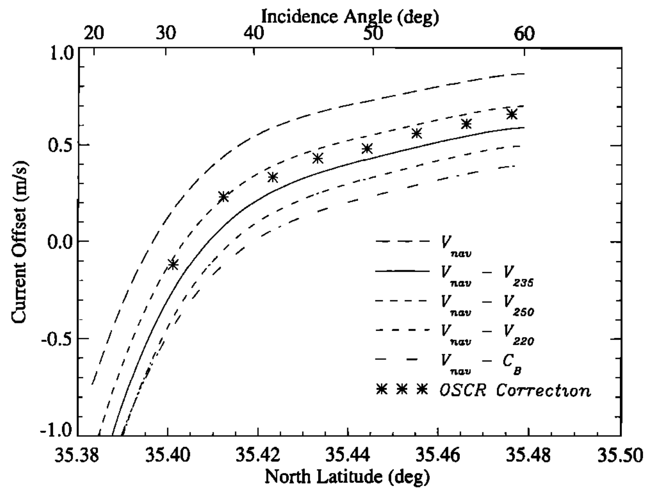

Figure 5. INSAR current offset versus latitude and incidence angle. The long-dashed curve, labeled V_{nav}, shows the correction due to navigational effects only. The curves labeled $V_{\text{nav}} - V_{\phi_w}$ show the full navigational and wave motion corrections for winds blowing from the indicated directions. The curve labeled $V_{\text{nav}} - C_B$ shows the navigational and simple Bragg wave motion correction. The asterisks indicate the current offset derived from the OSCR data.

subtracted from V_{nav} would yield a total cross-track velocity trend in nearly perfect agreement with the "OSCR corrections." A value of 242°T for the wind direction is certainly within the error bounds on the buoy wind measurements.

From the discussion presented in section 3.2, it is clear that calibrating the INSAR system is a complicated process. A precise method to determine the navigational phase trend, either using a land reference as described here or by onboard GPS techniques, is an absolute necessity. As we have described above, even with this navigational trend accurately determined, one must still account for the effect of surface-wave motion and wind drift. We have seen how small uncertainties in the wind-drift velocity, the wind direction, and/or the spreading width of the surface wave spectrum can lead to differences in the mean Doppler velocity as a function of range (or incidence angle) of the order of 0.2 m s^{-1}. Without additional surface current measurements (either in situ or from another remote-sensing device such as OSCR) one probably cannot hope for better accuracy than this in absolute velocity measurements from INSAR.

For the overflights of the High-Res experimental area on June 20, 1993, such additional measurements from the OSCR system were in fact available for improving the accuracy of the INSAR system's absolute velocity measurements; namely, the "OSCR correction" points shown in Figure 5. As mentioned previously, the dependence on latitude of the "OSCR correction" is essentially the same as that displayed by the wind-dependent correction curves. Thus the proper range correction can be easily determined simply by scaling the wind-dependent mean velocity contribution in such a way that when this scaled contribution is subtracted from the navigation correction, the resultant curve passes through the OSCR correction points. Because of the similarity between the two curves, only one OSCR measurement is needed to determine the proper scaling factor. Using the V_{235} mean Doppler velocity, we find that an almost perfect fit to the "OSCR correction" in Figure 5 is

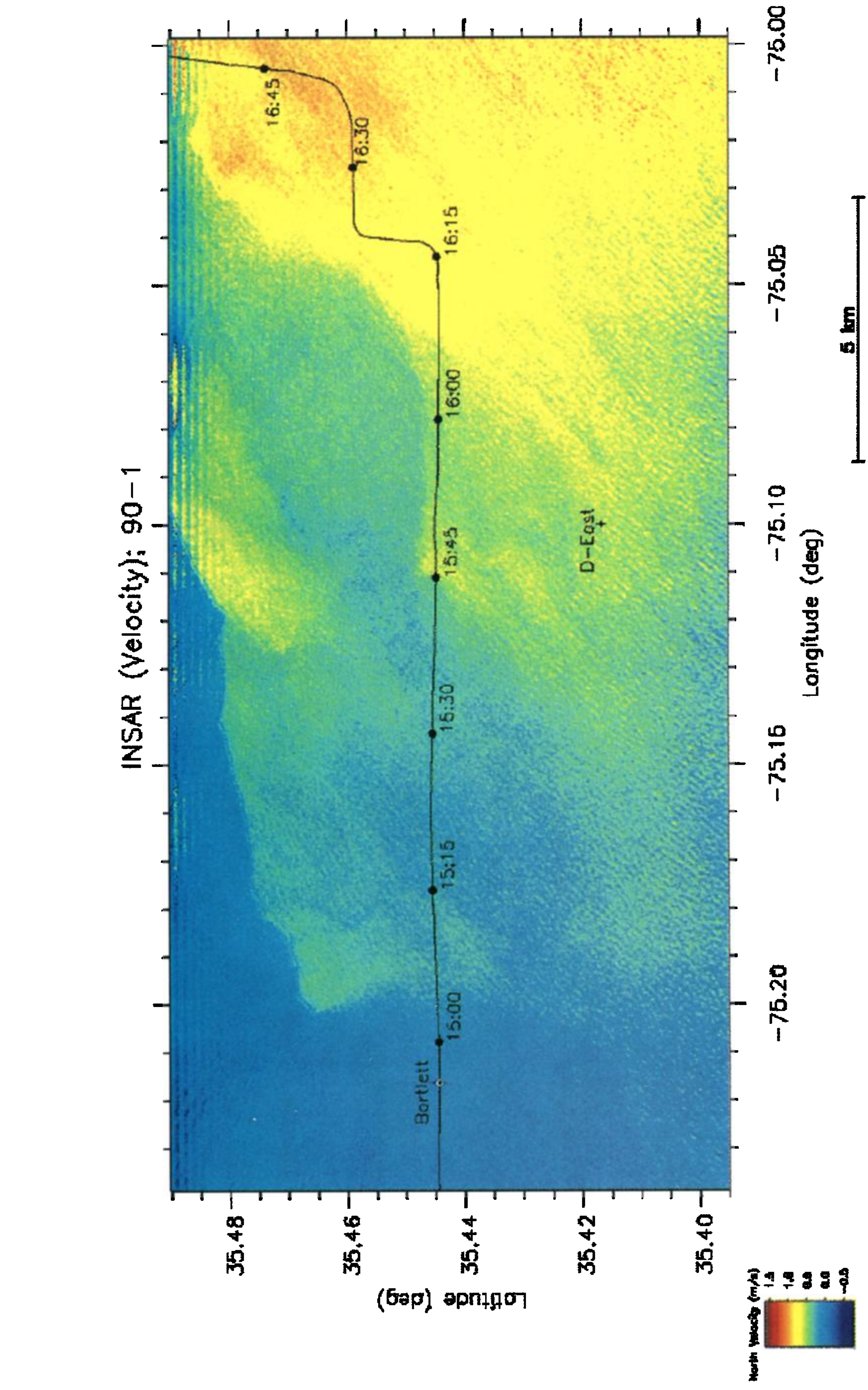

Plate 1. Image of the north surface velocity component for INSAR pass 90-1 collected at 1456 UT on June 20, 1993. The location and track of the research vessel *Bartlett* are shown for reference as well as the position of the DE (labeled D-East) wave buoy.

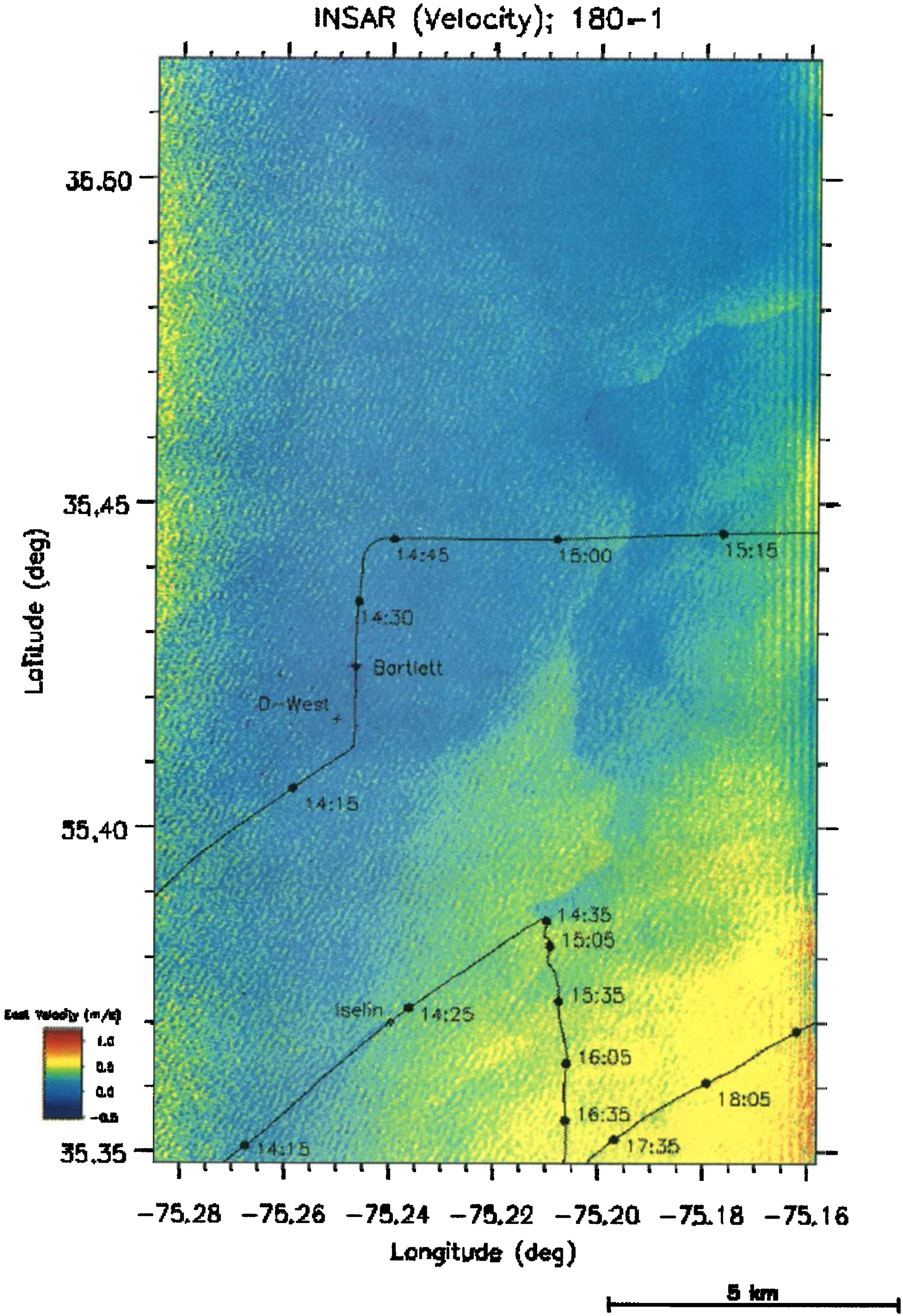

Plate 2. Image of the east velocity component for INSAR pass 180-1 collected at 1424 UT on June 20, 1993. The locations and tracks of the research vessels *Bartlett* and the *Columbus Iselin* are shown for reference as well as the position of the DW (labeled D-West) wave buoy.

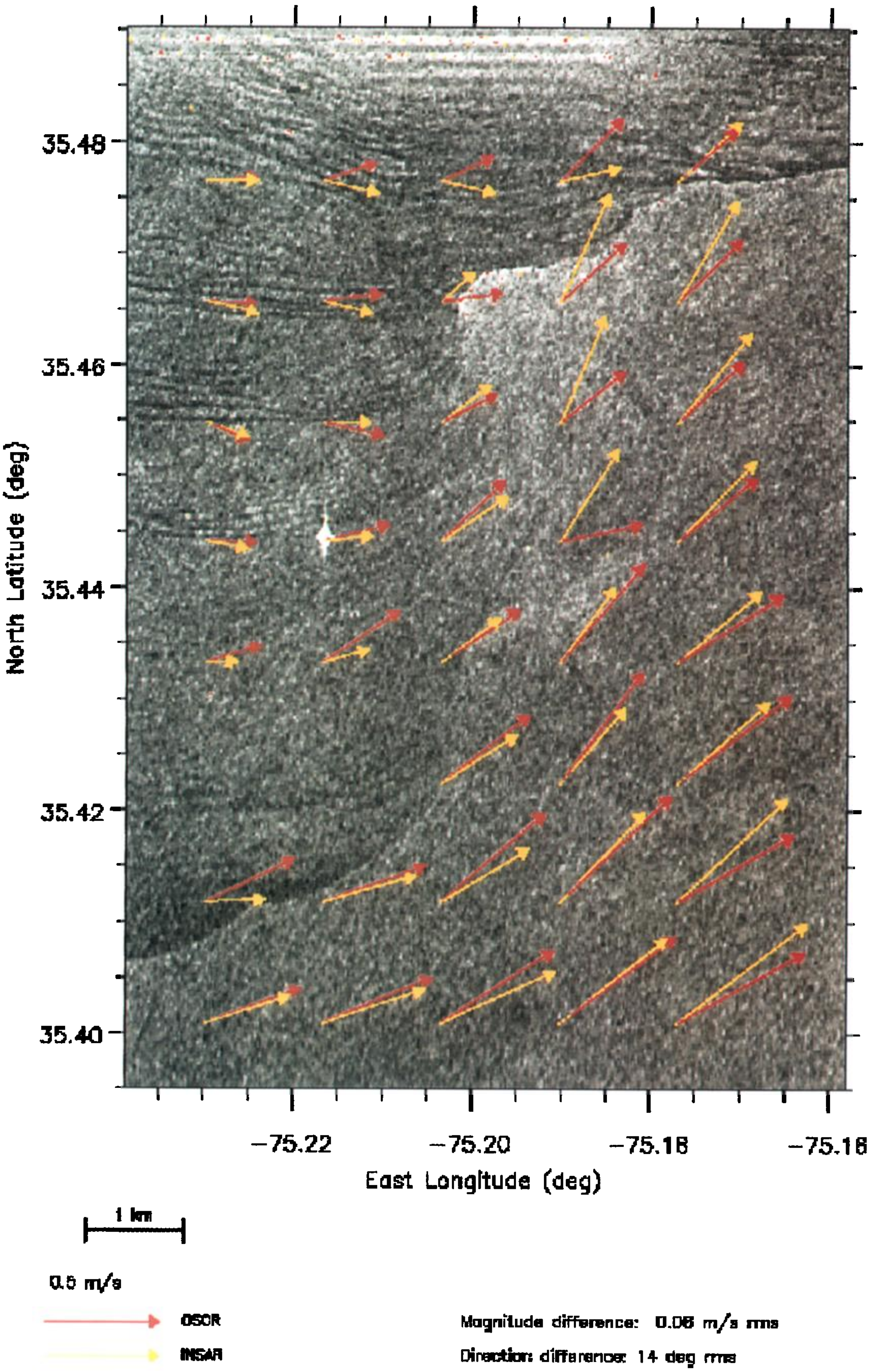

Plate 3. Comparison of the full surface current vectors (yellow arrows) constructed using the east component INSAR measurements from the 180-1 pass collected at 1424 UT and the north component measurements from the 90-1 pass collected at 1456 UT with the OSCR current vectors (red arrows) collected during these times. The vectors are overlayed on the common section of the eastbound INSAR magnitude image of Figure 6.

obtained with the curve $V_{nav} - 0.75V_{235}$. If a wind drift of 0.1 m s^{-1} is included, then an equally good fit can be obtained from the curve given by $V_{nav} - 0.4V_{235} - 0.1$. We have applied this latter form to correct the INSAR velocities for the 90-1 pass.

For many applications where INSAR velocity measurements might be desirable (e.g., open ocean), extensive in situ or OSCR-type velocity measurements over the entire area of interest will probably be unavailable. On the basis of the results presented here, an accurate range correction would nevertheless still be possible if one has a good estimate of the wind speed and direction (along with an accurate navigational correction) and even a single independent surface current velocity measurement as a "tie point." This is possible, because the trend of the mean Doppler velocity with range as predicted from our scattering model, at least for the 90-1 pass, appears to agree quite well with the trend measured by the OSCR. Therefore only a single independent velocity measurement is required to determine the proper scaling factor for the mean Doppler velocity trend. In cases such as the 180-1 INSAR pass in this study where accurate GPS navigational corrections are not available and where no land reference exists for computing such corrections, several independent current measurements across the range extent of the image are required. We have corrected the INSAR east-velocity components from pass 180-1 in our study with this procedure using the longitude dependence of the OSCR east component measurements at the fixed latitude position of 35.36°.

4. Surface Current Measurements on June 20, 1993

4.1. Description of Mesoscale Ocean Feature

In this section we discuss the oceanography of the region where comparisons between the INSAR surface currents and those from OSCR and various in situ sensors were made. This region, shown in Figure 1, is located near the inshore edge of the Gulf Stream's North Wall off Cape Hatteras, North Carolina, where heavier (saltier) water associated with the Gulf Stream collides with lighter (fresher) coastal water and produces rather sharp (100 m wide or so) zones of strong current gradients along the boundary of these two water masses. Such a feature existed on June 20, 1993, in the central part of the OSCR domain. The length of this "knee-like" but undulating surface feature was approximately 25 km, and the width was of the order of 100 m. A second, but weaker, feature, similar in shape and displaced about 5 km south, was also imaged by both SAR modes. Both features were traversed by the *Bartlett*, which collected extensive hydrographic measurements of the flow and water properties in their vicinity (G. O. Marmorino et al., Correlation of oceanographic signatures appearing in SAR and INSAR imagery with in situ measurements, manuscript in preparation, 1996; hereinafter referred to as Marmorino et al., manuscript in preparation, 1996).

In Figure 6 we show the INSAR magnitude image from the 90-1 flight leg. Each pixel in this image contains the value of $|R(\tau)|$ given by (9). This image is basically equivalent to a standard strip-map SAR image. (Note, with $\tau = 0$ in (9), the equivalence becomes exact.) We have superimposed on this image the track of the research vessel *Bartlett* as it traversed this area. The bright spot labeled *Bartlett* in the image marks the position of the research vessel at the imaging time of 1456 UT. The position of the wave buoy DE (labeled D-East) is also shown in the image. On the basis of hydrographic measurements from the *Bartlett*, we believe that the two undulating features seen in the image of Figure 6 define the boundary between different water masses as discussed above. Current gradients across these features caused by the subduction of the heavier water beneath the lighter can modulate the surface wave spectrum and hence the radar cross section in the vicinity of the features. In the upper left corner of this image, southward propagating internal waves are also observed.

We show the INSAR magnitude image for the 180-1 flight leg in Figure 7. As in Figure 6, the track of the *Bartlett* and the location of the DW (labeled D-West) wave buoy are indicated. Also, in Figure 7 the track of the other research vessel *Columbus Iselin* is overlaid. The bright points, labeled "Bartlett" and "Iselin," mark the positions of the two ships at the image collection time (1424 UT). This image clearly shows the extension of the north-south feature seen in the image of Figure 6. The internal wave signatures are less prominent in Figure 7, and only those waves near the northern boundary that seem to be propagating to the west or west-southwest are visible. This difference in the internal-wave signature in the two images results from the fact that the modulation of the surface-wave spectrum by internal waves depends on the gradient of the surface current [*Thompson et al.*, 1988]. This gradient usually exists only along the propagation direction. Finally, one should note that there is a region of overlap between the two images that encompasses the 90-1 image from its western boundary eastward to a longitude of about −75.14°E. In this region of overlap we can construct a vector velocity field using the phase portion of the two INSAR measurements. These measurements are discussed in the following subsection.

4.2. Comparison of OSCR and INSAR Currents

As discussed above, the magnitude of the autocorrelation function measured by the INSAR system is quite similar to usual strip-map SAR imagery. The additional information provided by the INSAR measurements comes from the phase, $\phi\{= \arg[R(\tau)]\}$, of the autocorrelation function. As discussed in subsection 3.2, these pixel-by-pixel phase measurements can, with appropriate processing and calibration, be converted to the horizontal surface current component along the INSAR look direction. Plate 1 depicts the north component of the surface current velocity as inferred from the INSAR phase measurements (90-1) corresponding to the magnitude image shown in Figure 6.

Plate 2 shows the east component of the surface current velocity (180-1 flight leg) corresponding to the magnitude image shown in Figure 7. As one expects, the features appearing in these velocity-component images are quite similar to those seen in the magnitude images described earlier. In particular, the water-mass boundaries can be clearly seen. Note also that the north component of the surface velocity shows a generally increasing trend from west to east across the image in Plate 1 with values greater than 1 m s^{-1} near the eastern edge. These values are consistent with velocities one would expect near the edge of the Gulf Stream located about 10 km or so east of the eastern edge of the image. Also, peak-to-trough surface current variations associated with the internal waves seen at the western edge of Plate 1 are about 0.1 m s^{-1}.

We are now in position to compare the surface currents inferred from the INSAR measurements with those measured by OSCR. Since the intrinsic resolution of OSCR is about 1 ×

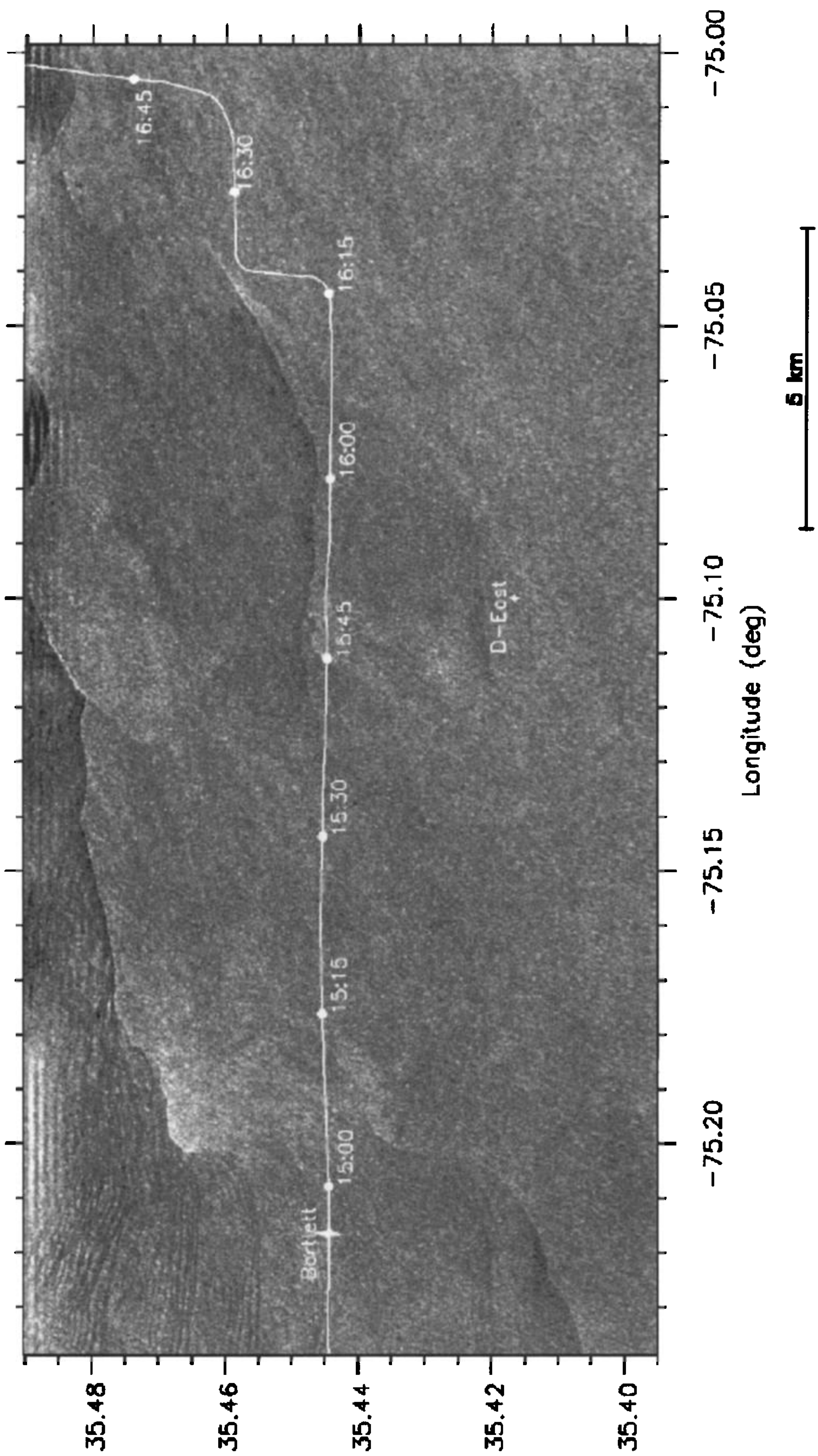

Figure 6. Magnitude image for INSAR pass 90-1 collected at 1456 UT on June 20, 1993. The location and track of the research vessel *Bartlett* are shown for reference as well as the position of the DE (labeled D-East) wave buoy.

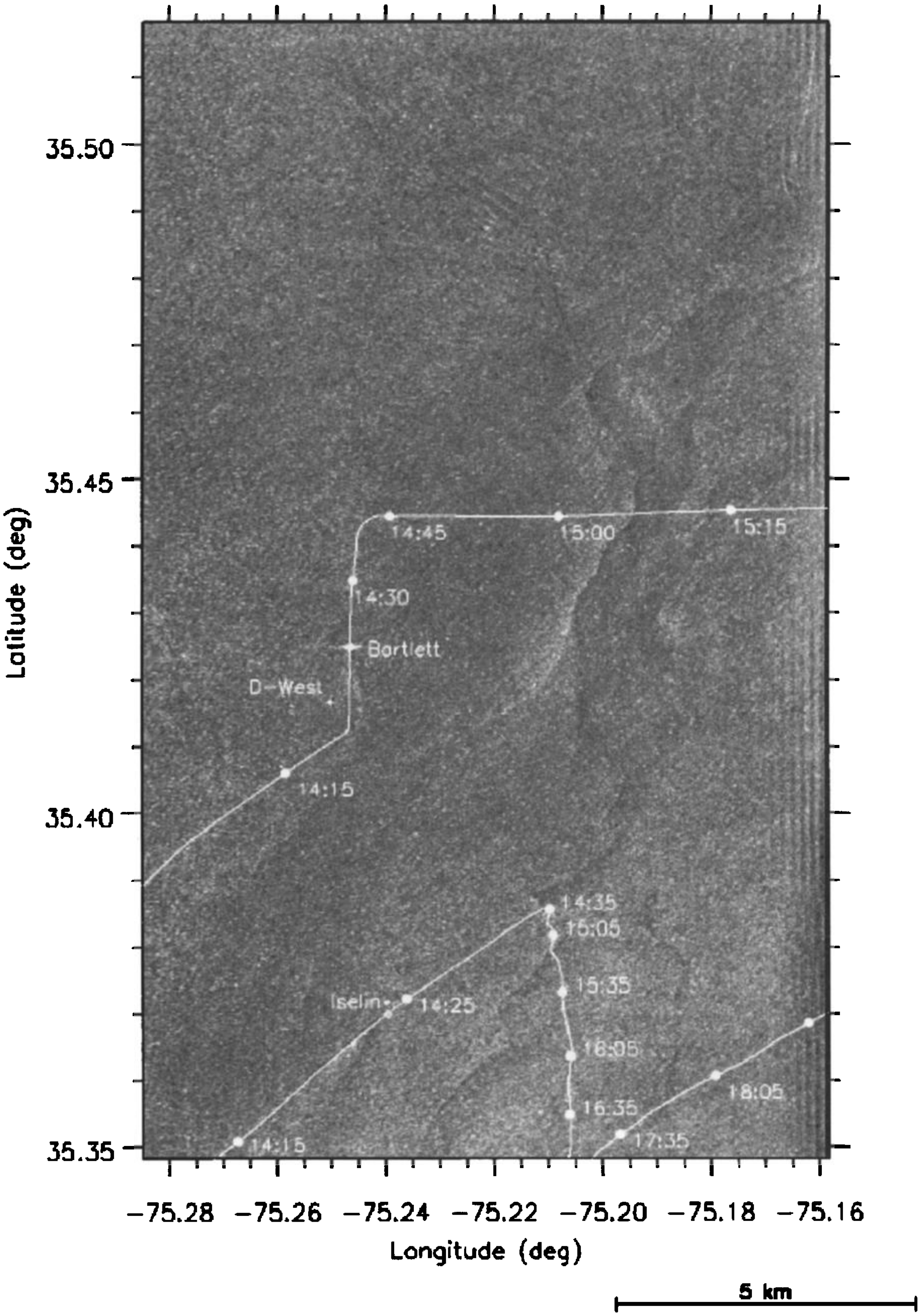

Figure 7. Magnitude image for INSAR pass 180-1 collected at 1424 UT on June 20, 1993. The locations and tracks of the research vessels *Bartlett* and *Columbus Iselin* are shown for reference as well as the position of the DW (labeled D-West) wave buoy.

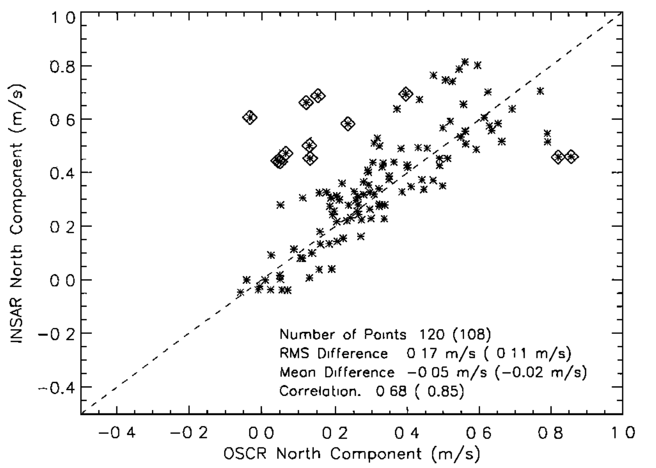

Figure 8. Scatterplot comparing the north velocity component measured by the OSCR and INSAR systems in the area imaged during INSAR pass 90-1. The rms difference for the entire sample is 0.17 m s^{-1}. When the outlier points labeled by diamonds are excluded from the sample, the rms difference is reduced to 0.11 m s^{-1}.

1 km compared to the roughly 10 × 10 m resolution of the INSAR system, we have smoothed the INSAR current images over a 1 × 1 km area centered around each of the OSCR measurement points. This procedure yields a one-to-one correspondence between the relevant INSAR-derived current components (the north components from the 90-1 flight leg of Plate 1 and the east components from the 180-1 flight leg of Plate 2) and the corresponding OSCR-derived surface current components. It is important to mention that since there was no land in the INSAR 180-1 imagery, we were not able to determine the navigational phase correction for this pass as described in section 3.2.1 for the 90-1 flight leg. On the basis of the findings in section 3.2 we have determined the total cross-track velocity trend by using the OSCR data appropriate to this pass.

In Figures 8 and 9 we present scatterplots of the north and east INSAR velocity components, respectively, averaged as described in the preceding paragraph and plotted against the corresponding OSCR components. For each of these plots we have used the OSCR measurements corresponding to the time closest to the appropriate INSAR flight leg (namely, 1500 UT for 90-1 and 1440 UT for 180-1). The rms difference, the mean difference, and the correlation coefficient between the OSCR and the INSAR measurements are listed in the plots. One can see that there is considerably more scatter in the north component values than in the east component values. At present we are not sure why this is the case. We have found, however, that the outlier points, marked by diamonds in Figure 8, where the respective components differ by more than 0.3 m s^{-1} generally occur at the far range of the OSCR system. It is possible that the there is a power deficiency for these OSCR range cells. As discussed by Chapman et al. (submitted manuscript, 1996) and Graber et al. (submitted manuscript, 1996), the error in the estimate of the velocity component normal to the radials from the two OSCR stations becomes larger as the angle between these radials becomes smaller. Thus it also quite likely that the larger scatter in the north component values is at least partially a result of the particular geometry of the OSCR system during the High-Res Experiment with respect to the location of the region imaged by the INSAR system. In these regions (see the map in Figure 1), geometrical arguments (Chapman et al., submitted manuscript, 1996; Graber et al., submitted manuscript, 1996) predict that the east components from the OSCR measurements should be about twice as accurate as the north components. Also, the location of these outlier points, in the upper right-hand corner of Plate 1, is where the current variations (as inferred by the INSAR and shown in Plate 1) are significant. It has been shown [*Thompson and Jensen*, 1993] that rapid variations in the surface current may lead to modulations of the surface wave spectrum that can ultimately degrade the performance of the INSAR system. In any case, when the 12 outlier points in Figure 8 are excluded from the sample, the values of the statistical parameters given in parentheses in the figure are considerably improved and in fact are comparable to the parameters found in comparisons among various in situ current-measurement devices (Chapman et al., submitted manuscript, 1996; Graber et al., submitted manuscript, 1996).

Since the difference in collection time for the two orthogonal INSAR flight legs was only about 30 min, it is reasonable to assume that the large-scale structure of the surface current field should be nearly the same for the two passes. We can therefore combine the east velocity components collected from the southbound INSAR pass (at 1424 UT) with the north components from the eastbound pass (at 1456 UT) to yield an estimate of the full surface velocity vector in the region where the two images overlap and compare these vectors with the corresponding OSCR vectors in this region. The results of such a comparison are shown in Plate 3, where we have overlayed the measured current vectors from the OSCR system (red arrows) and the INSAR (yellow arrows) on the common section of eastbound INSAR magnitude image of Figure 6. As explained earlier, we have again averaged the INSAR components over a 1 × 1 km area to compensate for the coarser resolution of the OSCR system. One can see from Plate 3 that the agreement between the two current vectors is quite good with an rms difference in the magnitude and direction of the OSCR and INSAR vectors of 0.06 m s^{-1} and 14°, respectively. The OSCR current estimates at the two leftmost grid points at latitude 35.42°N were corrupted. Most of the large deviations

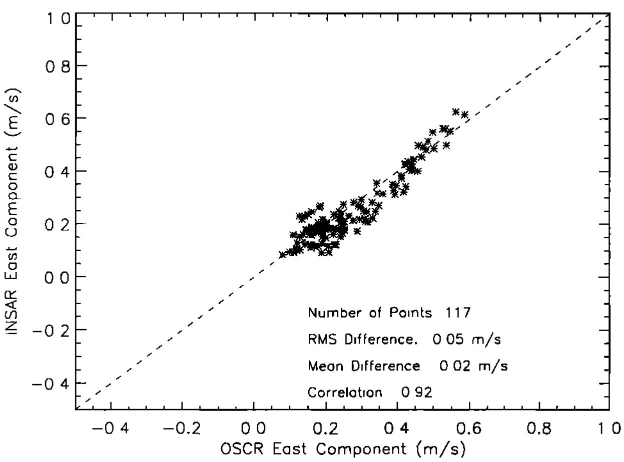

Figure 9. Scatterplot comparing the east velocity component measured by the OSCR and INSAR systems in the area imaged during INSAR pass 180-1. The rms difference for the entire sample is 0.05 m s^{-1}.

between the current vector estimates from the two systems are found generally in the vicinity of the water-mass boundary in the right center of the image. As mentioned above, this difference could be the result of surface wave modulation mechanisms that can affect the two systems differently or the motion of the boundary (comparable to the 1-km resolution cell) during the data collection period.

4.3. Current Variability in the Vicinity of the Frontal Feature

The comparisons between the OSCR and INSAR currents presented in the preceding paragraphs give us confidence that accurate measurements of ocean surface currents by interferometric SAR are indeed feasible if the proper corrections for navigation errors and surface-wave effects are performed. In this section we briefly discuss some examples of how high-resolution surface current maps might be used.

In Plate 4 we display the surface area common to both the 180-1 and the 90-1 INSAR overflights as in Plate 3 but this time with only the INSAR surface current vectors plotted on a 250-m grid. Again, we have overlayed these vectors on the common section of eastbound INSAR magnitude image of Figure 6. (Recall that the full resolution of the INSAR measurements is of the order of 10 m. We have plotted the current vectors in Plate 4 at 250-m resolution so that the underlying image is not obscured.) The complicated behavior of the surface current flow is easy to see from Plate 4. Note, in particular, the flow pattern in the vicinity of the water-mass boundary, especially near the "knee" in the upper center of the image. In this region the direction of the surface current changes abruptly from easterly on the west side of the boundary to northerly on the east side. Also apparent from Plate 4 is the converging nature of the current field along the northern (east-west oriented) section of the boundary.

The general behavior of the flow pattern shown in Plate 4 is consistent with the oceanography of the region as determined from detailed hydrographic measurements collected from the research vessels during the imaging period. These measurements indicate that there are three different water masses in the region, increasing in density toward the east and separated by the features apparent in the magnitude imagery (Marmorino et al., manuscript in preparation, 1996). The intermediate density water mass is bounded on the north by the bright east-west feature at the north and the dimmer more diffuse feature that roughly parallels the ship track in Figure 6. The high-resolution surface current map in Plate 4 clearly shows the different flow patterns in the three regions.

To our knowledge a calibrated area-extensive high-resolution surface current map such as that shown in Plate 4 has until now not been available. The availability of such maps opens a broad range of research possibilities. As we discussed in the introduction, two-dimensional current maps are extremely important for understanding wave-current interaction effects which ultimately produce the intensity modulations in microwave images of the ocean surface. With a knowledge of two-dimensional surface current field one will be able to examine more precisely the physics that governs the modulation mechanism. Furthermore, when this imaging mechanism is well enough understood, it may even be possible to deduce information about bulk properties of the water column based only on the surface measurements and model calculations. We plan to examine these possibilities in future studies using the extensive ground truth available in the High-Res data set.

5. Summary and Discussion

In this paper we have shown comparisons between surface current measurements from a shore-based HF radar system and an airborne interferometric SAR system. These comparisons show very good agreement between the current fields inferred from the two measurement techniques. Since the currents from the HF system have been found to be in agreement with in situ measurements from shipboard ADCPs and buoy-mounted current meters (Chapman et al., submitted manuscript, 1996; Graber et al., submitted manuscript, 1996), it follows that the INSAR measurements are also reliable. In fact, the comparisons presented in this paper provide the first quantitative validation that an INSAR system is indeed capable of accurate high-resolution current measurements.

The basic physics that underlies the OSCR and the INSAR current measurement techniques has been reviewed. In particular, we have shown how accurate current extraction from the INSAR system is critically dependent not only on precise navigation of the radar platform but also on the motion induced by longer-scale surface waves and wind that can advect the short-scale Bragg waves and bias the estimated current field. In our study we have used a portion of the INSAR flight leg that passed over the narrow strip of the Outer Banks to remove a range-dependent navigational bias in the INSAR phase image. The navigational correction was accomplished by simply forcing the phase of this (stationary) strip of land to have zero phase. Using meteorological and surface wave information from two buoys in the area as input into a microwave scattering model, we were then able to compute the Doppler velocity induced by the motion of the longwave field. Proper application of these two corrections to the measured INSAR phase image yields the final INSAR current field. We were able to check the consistency of the phase correction trend determined in this manner by comparing it with a trend determined solely from the OSCR measurements. The close agreement of these two trends provides additional confidence in our models as well as the extracted INSAR current field.

We have compared the OSCR current field with that extracted from the INSAR imagery and averaged over 1-km square pixels centered at the location of the OSCR measurements. North and east INSAR velocity components were determined from two orthogonal flight legs separated in time by about 30 min. In each case the comparisons were excellent. The rms difference in the north velocity components was 0.17 m s^{-1} (0.11 m s^{-1} with outliers removed) and was only 0.05 m s^{-1} in the east components. We suspect that the larger rms difference for the north components may be due to the presence of large current gradients in the north component image and possibly multiple or less resolved peaks in the OSCR Doppler spectra. With the assumption that the large-scale surface current field does not change too much during the 30 min between the orthogonal INSAR flight legs, we have used the common region of the corresponding images to infer a vector INSAR velocity in this region. Comparison of this velocity vector (again averaged over 1 km) with the appropriate OSCR vectors yields an rms magnitude difference of 0.06 m s^{-1} and an rms direction difference of 14°. As before this agreement is excellent.

In this study we have proposed two independent methods for calibration of the INSAR so that accurate absolute surface currents can be derived and have tested the validity of each of them using OSCR derived currents and other ground truth

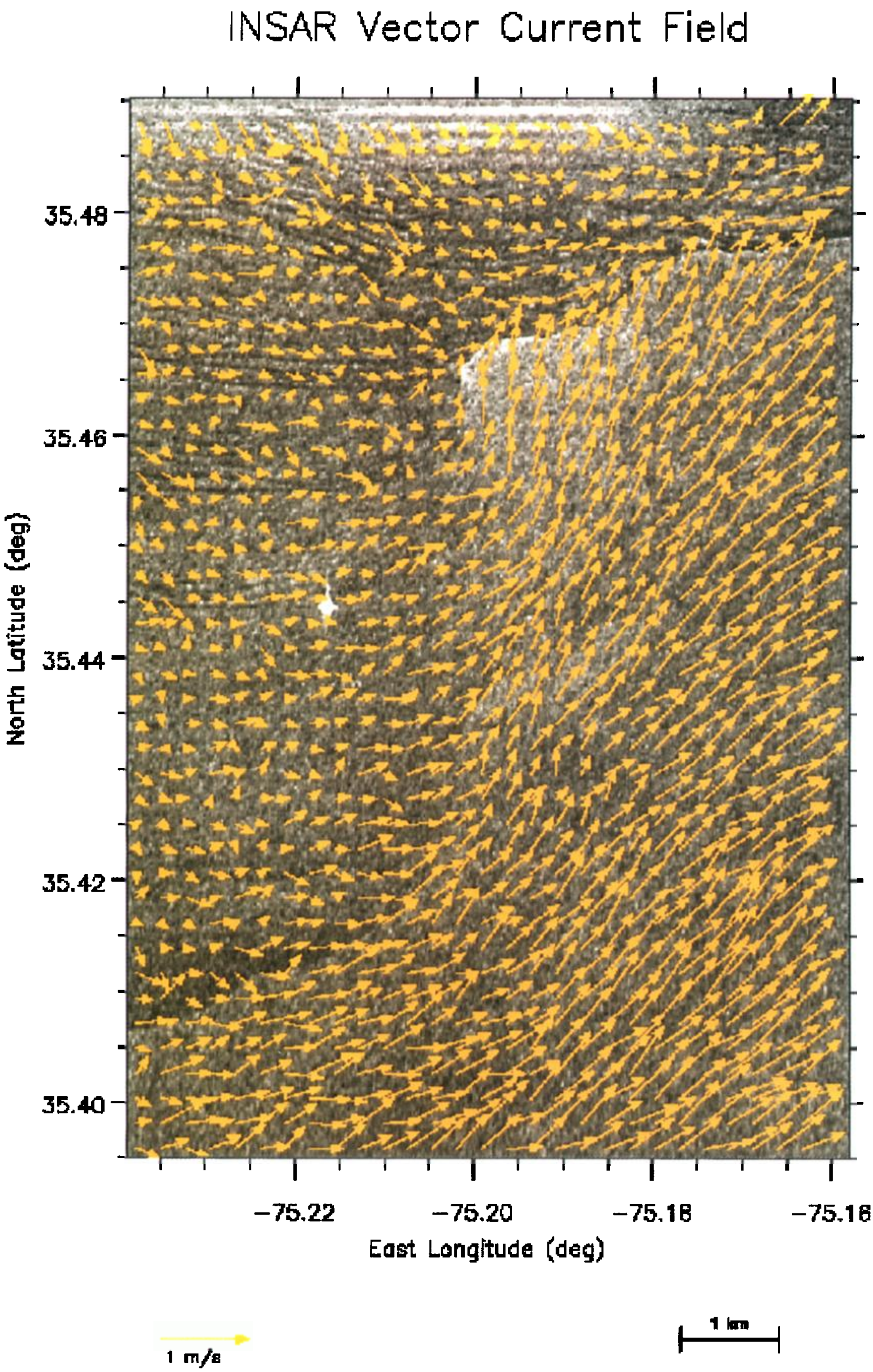

Plate 4. INSAR surface current vectors plotted at 250-m intervals using the east component INSAR measurements from the 180-1 pass collected at 1424 UT and the north component measurements from the 90-1 pass collected at 1456 UT and overlayed on the common section of the eastbound INSAR magnitude image of Figure 6.

collected during the course of the High-Res Experiment. The first method requires knowledge of surface gravity wave- and wind-induced motions as well as accurate platform navigation. To account properly for the wind and wave effects, in situ observations of the wind stress or equivalently the relevant parameters characterizing the marine boundary layer [e.g., *Donelan*, 1990] and the directional wave spectrum must be known. When such knowledge is available, we have shown how one can, in principle, use a microwave scattering model to calibrate the INSAR with no requirement for additional reference current measurements. In practice, uncertainties in the wind and wave field (as well as the scattering model) will usually require an additional in situ current measurement in order to achieve absolute calibration of the INSAR system. Generally, both wind and wave conditions can be assumed to remain steady and homogeneous over a few hours and tens of kilometers so that one measurement within the image will be sufficient to compute the wave motion and wind drift effects. For the case discussed in our study, these uncertainties may be approximately accounted for by a 10° change in the buoy-measured wind direction. We expect that INSAR calibration in the presence of an atmospheric front, strong bathymetric features in shallow water influencing the surface wave characteristics, and/or turbulent, gusty winds actively generating wind waves within the INSAR image will require more than a single in situ current observation.

The second calibration method is simpler and does not require the detailed knowledge of the wind and wave field. This method does, however, require several OSCR (or in situ) surface current measurements spaced along the range direction of the INSAR image from which one may infer the total cross-track velocity trend that must be removed from the INSAR phase. The drawback of this method is that the required additional current measurements, at least for OSCR-type HF systems, are limited to near coastal situations. The form of cross-track velocity trend determined from the OSCR currents in the present study suggests that it may be possible to characterize it by a simple analytic function dependence which would depend on the radar frequency and the wind and wave conditions. If this simple characterization could indeed be found, a single, near-surface current measurement would then be adequate to scale the INSAR calibration curve.

6. Conclusions

The main purpose of this paper is to demonstrate the capability of measuring surface vector currents with an airborne interferometric SAR system. We have presented two approaches to facilitate calibration of the INSAR phase maps and thus make this remote-sensing technique a viable option for acquiring surface currents in regions with strong current gradients and where high-resolution and area-extensive measurements are required. It is shown that INSAR phase maps collected over the experimental region agree qualitatively with the appropriate vector current fields derived from the OSCR HF radar system. In particular, both systems measured a gradual increase in current speed from nearshore eastward into the Gulf Stream. Furthermore, both instruments indicated variable currents in the vicinity of the frontal boundaries. A comparison of INSAR and OSCR currents shows rms differences of 0.17 (0.11) and 0.05 m s^{-1} for the north and east velocity components, respectively. The rms differences for the vector currents collected from the common region of two orthogonal INSAR flight legs are 0.06 m s^{-1} and 14° for speed and direction, respectively. A high-resolution INSAR vector current map derived from the orthogonal passes is also constructed. This map clearly shows the complicated flow field associated with the collision of coastal and Gulf Stream water masses. The INSAR-derived vector currents are consistent with in situ measurements along the water mass boundaries and with the currents from OSCR.

We believe that the results presented in this paper provide the first quantitative demonstration based on concurrent in situ measurements that INSAR systems can provide realistic high-resolution current maps that should be extremely useful for many oceanographic applications. The INSAR promises to become a valuable tool for the oceanographic community, and its capabilities will permit examination of spatially varying processes with great detail. The present effort is just the beginning in the verification and analysis of the INSAR characteristics; more process-oriented experiments such as High-Res are needed to establish its range of application and to make INSAR current measurements more routine. Ultimately, we believe that the INSAR approach, perhaps even from a satellite-based platform, can provide operationally accurate and very high resolution current measurements of the coastal ocean.

Acknowledgments. The first two authors gratefully acknowledge funding support by the Office of Naval Research (ONR) under grants N00014-91-J-1775 and N00014-95-1-0046, respectively. The authors extend special thanks to Michael VanWoert and William Patzert, formerly at the National Aeronautics and Space Administration (NASA), and C. Linwood Vincent of the U.S. Army Corps of Engineers for their support in making the INSAR flight possible. We also appreciate the support provided by Fuk Li at JPL for processing this data set. We are grateful for the stimulating comments from our colleagues George Marmorino (NRL) and Rick Chapman (JHU/APL) and to Slavica Nikolic for work on some of the graphics. Finally, we are thankful to Nick Shay (RSMAS) for seeing through the OSCR measurements.

References

Ainsworth, T. L., S. R. Chubb, R. A. Fusina, R. M. Goldstein, R. W. Jansen, J.-S. Lee, and G. R. Valenzuela, INSAR imagery of surface currents, wave fields, and fronts, *IEEE Trans. Geosci. Remote Sens.*, *33*(5), 1117–1123, 1995.

Anctil, F., M. A. Donelan, G. Z. Forristall, K. E. Steele, and Y. Oullet, Deep water field evaluation of NDBC/SWADE 3-meter discus directional buoy, *J. Atmos. Oceanic Technol.*, *10*(1), 97–122, 1993.

Barrick, D. E., M. W. Evans, and B. L. Weber, Ocean surface currents mapped by radar, *Science*, *198*, 138–144, 1983.

Beal, R. C., P. S. DeLeonibus, and I. Katz, *Spaceborne Synthetic Aperture Radar for Oceanography*, *Johns Hopkins Oceanogr. Stud.*, 7, 215 pp., 1981.

Beal, R. C., V. Kudryavtsev, D. R. Thompson, S. Grodsky, D. G. Tilley, V. Dulov, and H. C. Graber, The influence of the marine atmospheric boundary layer on ERS 1 synthetic aperture radar imagery of the Gulf Stream, *J. Geophys. Res.*, in press, 1996.

Carande, R. E., Estimating ocean coherence time using dual-baseline interferometric synthetic aperture radar, *IEEE Trans. Geosci. Remote Sens.*, *32*(4), 846–854, 1993.

Cimino, J. B., and C. Elachi, The Shuttle Imaging Radar A (SIR-A) Experiment, *JPL Publ.*, *82-77*, 5–53, 1982.

Cimino, J. B., B. Holt, and A. H. Richardson, The Shuttle Imaging Radar B (SIR-B) Experiment Report, *JPL Publ.*, *88-2*, 218 pp., 1988.

Crombie, D. D., Doppler spectrum of sea echo at 13.56 Mcs^{-1}, *Nature*, *175*, 681–682, 1955.

Donelan, M. A., Air-sea interaction, in *The Sea*, vol. 9, *Ocean Engineering Science*, edited by B. LeMehaute and D. M. Hanes, pp. 239–292, Wiley-Interscience, New York, 1990.

Ford, J. P., J. B. Cimino, and C. Elachi, Space Shuttle Columbia views the world with imaging radar: The SIR-A Experiment, *JPL Publ.*, *82-95*, 144–145, 1983.

Ford, J. P., J. B. Cimino, B. Holt, and M. R. Ruzek, Shuttle imaging radar views the Earth from Challenger: The SIR-B Experiment, *JPL Publ., 86-10*, 135 pp., 1986.

Fu, L.-L., and B. Holt, SEASAT views oceans and sea ice with synthetic-aperture radar, *JPL Publ., 81-120*, 200 pp., 1982.

Gasparovic, R. F., J. R. Apel, D. R. Thompson, and J. S. Tochko, A comparison of SIR-B synthetic aperture radar data with ocean wave measurements, *Science*, *232*, 1529–1531, 1986.

Goldstein, R. M., and H. A. Zebker, Interferometric radar measurements of ocean surface currents, *Nature*, *328*, 707–709, 1987.

Goldstein, R. M., T. P. Barnett, and H. A. Zebker, Remote sensing of ocean currents, *Science*, *246*, 1282–1285, 1989.

Graber, H. C., T. N. Lee, B. K. Haus, C. G. H. Rooth, E. J. Williams, and L. K. Shay, Observations of ocean surface currents off the South Florida Keys using an Hf Doppler radar. SFOSRC/SEFCAR Pilot Field Study PFS-2: 14 May–13 June 1994, SFOSRC Technical Report, 175 pp., Univ. of Miami, Miami, Fla., 1995.

Herr, F., C. Luther, G. Marmorino, R. Mied, and D. Thompson, Ocean surface remote sensing program planned, *Eos Trans. AGU*, *72*(19), 214, 1991.

La Violette, P. E., D. R. Johnson, and D. A. Brooks, Sun-glitter photographs of Georges Bank and the Gulf of Maine from the space shuttle, *Oceanography*, *3*(1), 43–49, 1990.

Lee, T. N., Florida Current spin-off eddies, *Deep Sea Res.*, *22*, 753–765, 1975.

Lee, T. N., and D. A. Mayer, Low-frequency current variability and spin-off eddies along the shelf off southeast Florida, *J. Mar. Res.*, *35*(1), 193–220, 1977.

Marmorino, G. O., R. W. Jansen, G. R. Valenzuela, C. L. Trump, J. S. Lee, and J. A. C. Kaiser, Gulf Stream surface convergence imaged by synthetic aperture radar, *J. Geophys. Res.*, *99*(C9), 18,315–18,328, 1994.

Plant, W. J., Bragg scattering of electromagnetic waves from the air/sea surface, in *Surface Waves and Fluxes*, vol. 2, *Remote Sensing*, edited by G. L. Geernaert and W. J. Plant, pp. 41–108, Kluwer Acad., Norwell, Mass., 1990.

Scully-Power, P., Navy Oceanographic Shuttle Observations, STG-41G Mission Report, *NUSC Tech. Doc. 7611*, Nav. Underwater Syst. Cent., New London, Conn., 1986.

Shay, L. K., H. C. Graber, D. B. Ross, L. Chemi, N. Peters, J. Hargrove, R. Vakkayil, and L. Chamberlain, Measurements of ocean surface currents using an HF radar during High-Res-2, *RSMAS Tech. Rep. 93-007*, 66 pp., Univ. of Miami, Miami, Fla., 1993.

Shay, L. K., H. C. Graber, D. B. Ross, and R. D. Chapman, Mesoscale ocean surface current structure detected by HF radar: Data quality, *J. Atmos. Oceanic Technol.*, *12*(4), 881–900, 1995.

Shemer, L., M. Marom, and D. Markman, Estimates of currents in the nearshore ocean region using interferometric synthetic aperture radar, *J. Geophys. Res.*, *98*(C4), 7001–7010, 1993.

Stewart, R. H., and J. W. Joy, HF radio measurements of surface currents, *Deep Sea Res.*, *21*, 1039–1049, 1974.

Thompson, D. R., Doppler spectra from the ocean surface with a time-dependent composite model, in *Radar Scattering From Modulated Wind Waves*, edited by G. J. Komen and W. A. Oost, pp. 27–40, Kluwer Acad., Norwell, Mass., 1989.

Thompson, D. R., and J. R. Jensen, Synthetic aperture radar interferometry applied to ship-generated internal waves in the 1989 Loch Linnhe experiment, *J. Geophys. Res.*, *98*(C6), 10,259–10,269, 1993.

Thompson, D. R., B. L. Gotwols, and R. E. Sterner II, A comparison of measured surface-wave spectral modulations with predictions from a wave-current interaction model, *J. Geophys. Res.*, *93*(C10), 12,339–12,343, 1988.

Thompson, D. R., B. L. Gotwols, and W. C. Keller, A comparison of K_u-Band Doppler measurements at 20° incidence with predictions from a time-dependent scattering model, *J. Geophys. Res.*, *96*(C3), 4947–4955, 1991.

R. E. Carande, Vexcel Corporation, 2477 55th Street, Suite 201, Boulder, CO 80301.

H. C. Graber, Rosenstiel School of Marine and Atmospheric Science, University of Miami, 4600 Rickenbacker Causeway, Miami, FL 33149-1098. (e-mail: hans@cheyenne.rsmas.miami.edu)

D. R. Thompson, Applied Physics Laboratory, Johns Hopkins University, Johns Hopkins Road, Laurel, MD 20723-6099.

(Received February 16, 1996; revised June 17, 1996; accepted July 9, 1996.)